Journal of the Brazilian Society of Mechanical Sciences and Engineering (2023) 45:570
https://doi.org/10.1007/s40430-023-04492-4

TECHNICAL PAPER

Effects of body-armor-like grinding wheel parameters on surface quality and material removal rate in high-shear and low-pressure grinding process

Bing Liu[1] · Yebing Tian[1,2] · Jinguo Han[1,2] · Jinling Wang[1] · Guoyu Zhang[1] · Zhiqiang Gu[1]

Received: 13 September 2022 / Accepted: 13 September 2023 / Published online: 8 October 2023

Abstract

In the high-shear and low-pressure grinding process, the loose and small abrasive particles will agglomerate together to produce hydro-cluster effect, which drives the abrasive particles to remove the workpiece material. The liquid-body-armor-like grinding wheel parameters, especially, the abrasive fluid properties, have a direct influence on the hydro-cluster effect, which further determined the material removal efficiency and surface quality. Therefore, the experimental investigation was conducted to explore the effects of the abrasive type, size, and percentage on surface roughness *Ra* and material removal rate. To further explain the surface formation mechanism of the Inconel718 alloy workpiece, the autocorrelation function and the power spectral density function (PSD) of surface profiles was discussed. After the optimization of wheel parameters, the surface roughness *Ra* of Inconel718 alloy decreased from 0.3 to 0.094 μm. A material removal rate of 1.069×10^5 μm^3/mm·s was obtained as well. The PSD curve mainly concentrated in 0–40 k Hz, indicating that a bigger cluster elastomer of abrasive particles was generated in the grinding zone. Additionally, the variation of workpiece surface morphology has validated the grinding performance. The original pretreatment scratches were completely removed. A smooth surface was obtained after grinding. The experiment results verified that the optimized grinding wheel was effective for HSLP grinding of Inconel718 alloy.

Keywords Liquid-body-armor-like grinding wheel · High-shear and low-pressure grinding · Wheel parameters · Grinding performance · Surface formation mechanism

1 Introduction

Grinding is widely used as a finishing or near-finishing process due to low cost, high machining efficiency, and good quality [1–3]. During grinding process, numerous abrasives in a random distribution and with varied types, percentages, sizes, and shapes removal workpiece material in the form of tiny chips [1]. In the past several decades, advanced grinding-related mechanisms, methods, and systems, as well as various theoretical models have been proposed in the literatures.

Creep feed grinding (CFG) is usually used in machining superalloy components. In comparison to the conventional grinding methods, CFG has a higher material removal rate through the special feature of low workpiece speed and large depth of cut [4]. Numerous effects have been made to gain a more in-depth understanding of CFG. Hood et al. [5] conducted an experimental research on CFG using the single-layer electroplated diamond grinding wheel for the γ-TiAl alloy. The maximum G-ratio of ~ 100 and workpiece surface roughness *Ra* of 2.94 μm were reported. Normal and tangential forces were up to 2500 N and 500 N, respectively. Zhang et al. [4] reported an experimental investigation for IC10 grinding. The relationship of grinding parameters on the grinding force and the temperature was uncovered. Furthermore, the effects of workpiece surface roughness and hardening on the fatigue life of the specimens were clearly indicated. The findings provided a useful reference for

Technical Editor: Adriano Fagali de Souza.

✉ Yebing Tian
tianyb@sdut.edu.cn; tyb79@sina.com

[1] School of Mechanical Engineering, Shandong University of Technology, 266 Xincun West Road, Zibo 255049, Shandong, People's Republic of China

[2] Institute for Advanced Manufacturing, Shandong University of Technology, Zibo 255049, People's Republic of China

finetuning the grinding parameters. However, a variety of issues, e.g., increased grinding force, power consumption and grinding temperatures, remained to be addressed for the CFG process [3]. Ultra-high-speed grinding (UHSG) is an effective technique used in high-performance precision machining process. Grinding speed of 150–300 m/s or higher are required. To avoid a large mass loading imposed on the spindle, a wheel made of carbon fiber-reinforced polymer, which has a low density and high specific strength was reported. After optimizing the wheel structure, 400 m/s of grinding speed was reached [6]. Whereas, unpredictable broken failures have emerged at a faster speed, which limits its application. Wu et al. [7] assessed the accidental explosion of the bronze-bond CBN wheel in UHSG through fractography and numerical analysis. The causes of explosion were declared. The accident was attributed to the fatigue cracks which appeared along the interface between the bond and grain, adhesive failure at the interface between the wheel matrix and the abrasive layer, and defects which appeared at thread holes. To take advantages of CFG and UHSG, a newer high-efficiency deep grinding (HEDG) process is presented. A higher specific removal rate of 50 $mm^3/mm{\cdot}s$ was easily achievable whilst improving process efficiency and surface integrity [8]. However, the contact condition between the abrasive and chip was totally different with the high grinding speed, cutting depth, feed rate, and the thermal behavior. It is known that the high grinding temperature would deteriorate surface integrity of specimens. The interesting attempt for intermittent grinding (IG) was proposed to reduce grinding temperature and improve the grinding quality. In this process, the workpiece does not get continuously interacted with the wheel. A smaller grinding force and lower temperature were found due to the increased amount of coolants into the grinding zone [9, 10]. However, the extensive use of coolants was not recommended due to the raised health and environmental risk [11, 12]. More attention was focused on the minimum quantity lubrication (MQL) grinding technology in recent years [13]. The nanoparticle was creatively introduced to the MQL grinding to reduce the frictional force between abrasive and chip, thereby, improving the ground quality of workpiece [14]. However, despite its good lubrication, MQL cannot meet the grinding cooling requirement in term of temperature when compared to fluid grinding [15]. Improvement on novel grinding methods to solve the high grinding temperature and force are going on, especially for difficult-to-cut materials [16].

Shape-adaptive grinding (SAG) is a comparatively newer grinding process, in which a nanolevel surface roughness could be obtained. In SAG, an elastic body covered with pellets was reported [17]. Without a hard contact between the tool and workpiece, surface damage could be minimized. Moreover, based on multi-axis machine or robots, abrasive belt grinding process used for blades was operated. During grinding process, the hardness of the elastic body was important for influencing the grinding performance. Wang et al. [18]. revealed the positive-going relation between rubber wheel hardness and material removal, in which the normal grinding force remained unchanged. Xiao et al. [19]. explored the influence of process parameters on fatigue life after abrasive belt grinding. For GH4169 superalloy, the optimized machining parameters range was proposed to obtain the better fatigue performance. Furthermore, considering the limitations for difficult-to-machine materials, various hybrid processes, e.g., electrochemical deep grinding process, ultrasonic vibration-assisted grinding process, etc., have been developed to improve machine quality [20–22].

The aforementioned grinding methods are useful on improving the machining efficiency and ground surface quality. However, challenges of grinding chatter, grinding burn, and poor surface quality still existed [23]. Literatures have revealed that a larger negative angle of the abrasive grain is the root cause of the bigger normal grinding force during the conventional grinding process. [24]. Therefore, the high-shear and low-pressure (HSLP) grinding method using a newly developed liquid-body-armor-like grinding wheel was proposed to reduce the normal force and increase tangential force [25–27]. In our previous studies, the design of the new liquid-body-armor-like grinding wheel was described, which introduced the abrasive grain into the STF treated fabrics [27]. The material removal principle of the HSLP grinding process using the developed wheel has been illuminated as Fig. 1 according to our previous study [25]. When the wheel did not contact the workpiece, the dispersed phase (silica particles) and abrasive particles were uniformly dispersed. As the wheel contacted the workpiece at a high velocity, the abrasive layer impacted the micro-convex peak on the workpiece surface, as shown in Fig. 1(b). A large tangential load on the abrasive particle was generated instantaneously. Due to the shear thickening effect, the dispersed phase particle around the abrasive particle rapidly aggregated into particle clusters. Tangential holding force for abrasive was thus enhanced. The particle clusters held the abrasive to cut the peak when the critical yield stress of the workpiece was exceeded, as shown in Fig. 1(c). After that, the load on the abrasive was unloaded, and the particle clusters vanished. Simultaneously, the abrasive return to its original state. The HSLP grinding process is obtained by repeating the above steps. In the references [25] and [26], the principle of the novel HSLP method and the development process of the novel grinding wheel has been introduced. The rheology prosperity of the developed abrasive fluid was measured as well to display the high-shear and low-pressure effect. The machining ability was well validated by the experiment investigation. The effect of grinding parameters on the HSLP grinding performance was investigated in

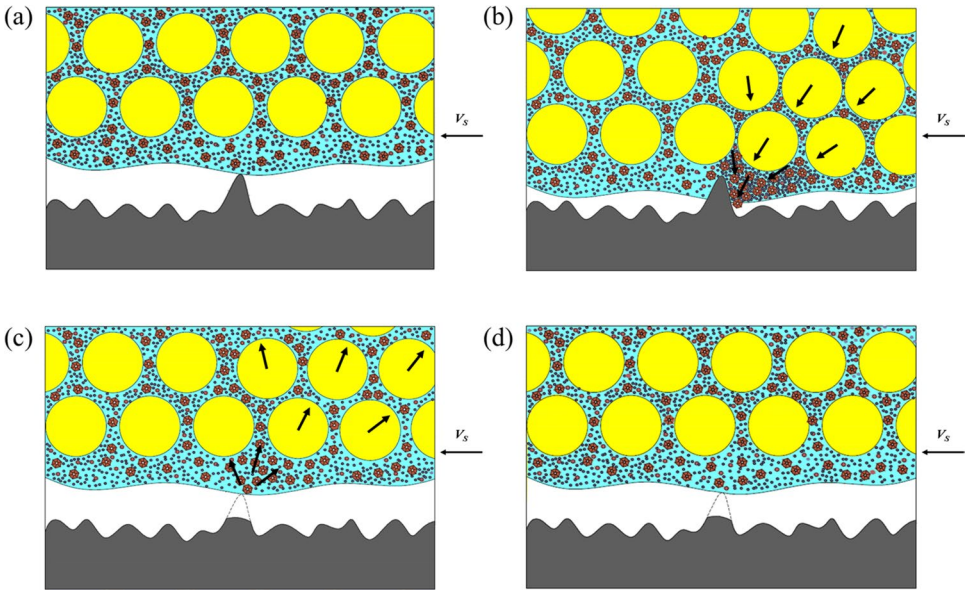

Fig. 1 Principle of HSLP grinding process: **a** initial stage, **b** contact stage, **c** material removal stage, and **d** recovery stage [25]

[27], where the optimal grinding parameters were obtained for the Inconel 718. However, how the abrasive material, particle size, and mass percentage of abrasive particle affect the grinding characteristics (grinding quality and material removal efficiency) is still unknown. Besides, the formation mechanism of workpiece surface has not been fully revealed.

To cover this gap, the preparation process of the liquid-body-armor-like wheel was illustrated in detail. A series of grinding experiments on different abrasive materials (Al_2O_3, SiC and CBN), size (1, 10, and 20 μm), and mass percentage (5, 10, and 15 wt%) were performed. The ACF and PSD method was used to explain the surface formation mechanism, rather than the 2D statical results. Based on the experimental and analysis results, the optimal wheel parameters were obtained to better guide the practice application.

2 Experimental details and methods

2.1 Materials

Abrasive layers of the novel liquid-body-armor-like grinding wheel include the hydrophilic fumed silica (particle size in 7–40 nm), polyethylene glycol (200 g/mol, PEG200, chemically pure, Newtonian fluid), ethyl alcohol absolute (mass fraction ≥ 99.7%), and polymer polyethylene fiber. The SiC particles, Al_2O_3 particles and CBN particles with average size of 1 μm, 10 μm, and 20 μm were served as the abrasive, respectively.

2.2 Abrasive layer preparation

The abrasive layer preparation flow is presented in Fig. 2, including the following steps:

Firstly, the STF was prepared. PEG200 was served as the base fluid. Fumed silica was added to the base fluid

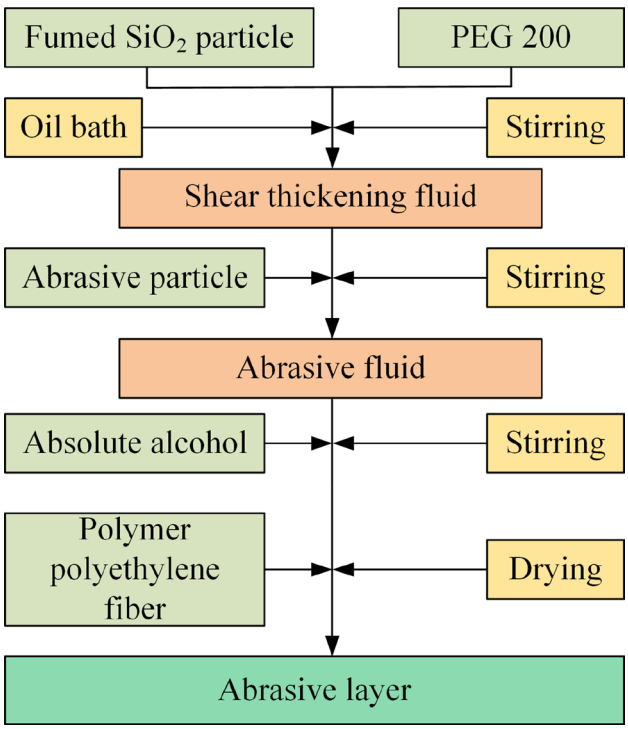

Fig. 2 Flow chart of the abrasive layer preparation

through the mechanical agitation, then the STF (solid contents 15 wt%) was obtained [27].

Secondly, the abrasive fluid was produced. Based on the fabricated STF, the abrasive particles were served as additive for the preparation of abrasive fluid.

Finally, the abrasive fluid was diluted by the anhydrous ethanol. The polymer polyethylene fabrics were immersed in the diluted abrasive fluid. The fabrics was then dried until the anhydrous ethanol was volatilized completely. After that, the abrasive layer was obtained.

The structure diagram of the liquid-body-armor-like grinding wheel is shown in Fig. 3. The Fig. 3(a) illuminates the configuration of the novel grinding wheel. It includes the abrasive layer and wheel matrix. The abrasive layer was wound on the matrix of the wheel and fixed mechanically. The dispersed phase particle, i.e., SiO_2 and abrasive are evenly dispersed in the STF, as displayed in Fig. 3(b). Figure 3(c) shows the structure of the warp-knitted spacer fabrics woven by the polymer polyethylene fibers, which exhibited the smooth surface. The polymer polyethylene fibers impregnated abrasive fluid, namely abrasive layer, as shown in Fig. 3(d).

2.3 Grinding conditions

Experiments were conducted to explore the effects of different wheel parameters (abrasive type, abrasive particle size, abrasive mass percentage) on the surface roughness *Ra* and material removal rate *MRR*. The experimental setup is presented in Fig. 4. All experiments were conducted on the SMART B818III grinder. The grinding wheel was prepared as the last section. Three types of abrasive particle, Al_2O_3, SiC, and CBN were investigated. 1, 10, and 20 μm of abrasive particle size were employed, respectively. The mass percentages in abrasive fluid adopted were 5 wt%, 10 wt%, and 15 wt%, respectively.

The Inconel718 alloy in the volume of 10 × 10 × 3 mm was machined. They were pre-machined by the conventional grinding wheel to ensure initial surface roughness of ~ 0.3 μm in all experiments. According to our previous works, the grinding parameters, grinding speed v_s, feed speed v_w, and cutting depth a_p were kept at 5 m/s, 500 mm/min, and 250 μm, respectively. Being different from the conventional grinding process, a_p was defined as the normal displacement between the initial point and the start grinding point of wheel. It should be noted that the initial point was the placement of wheel being about to touch workpiece before grinding, which could be judged effectively on the basis of the detected first-signal peak of the

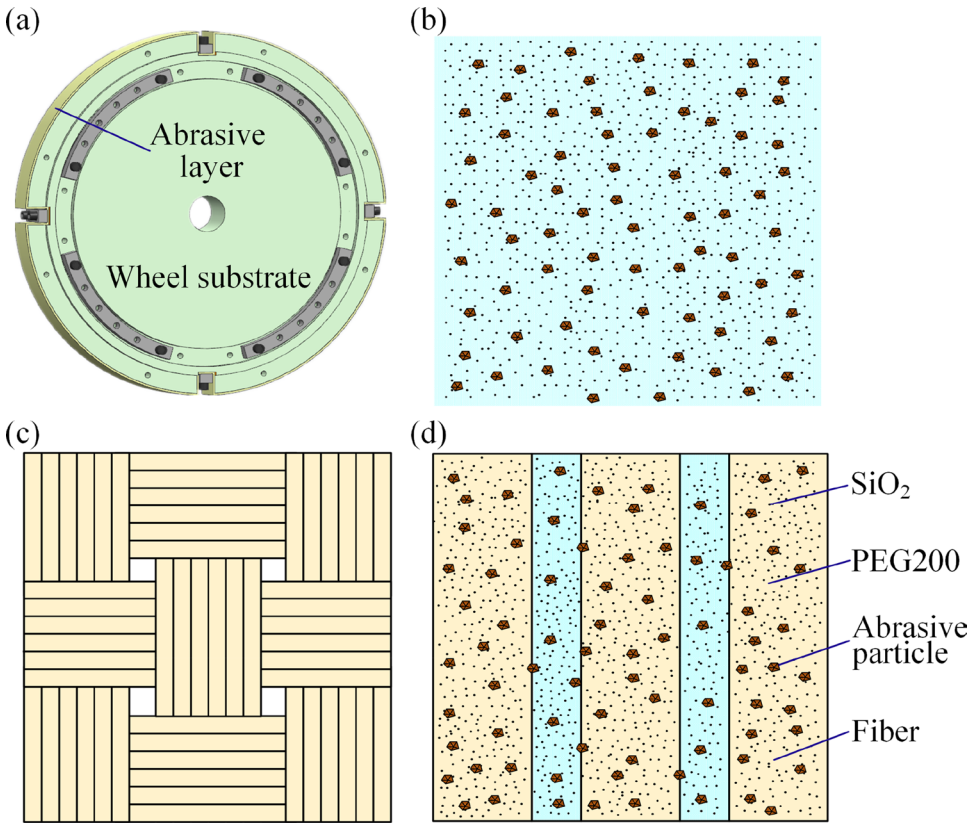

Fig. 3 Structure diagram of the new wheel: **a** configuration of the new wheel, **b** diagram of abrasive fluid, **c** structure of the fiber fabrics, **d** configuration of the abrasive layer

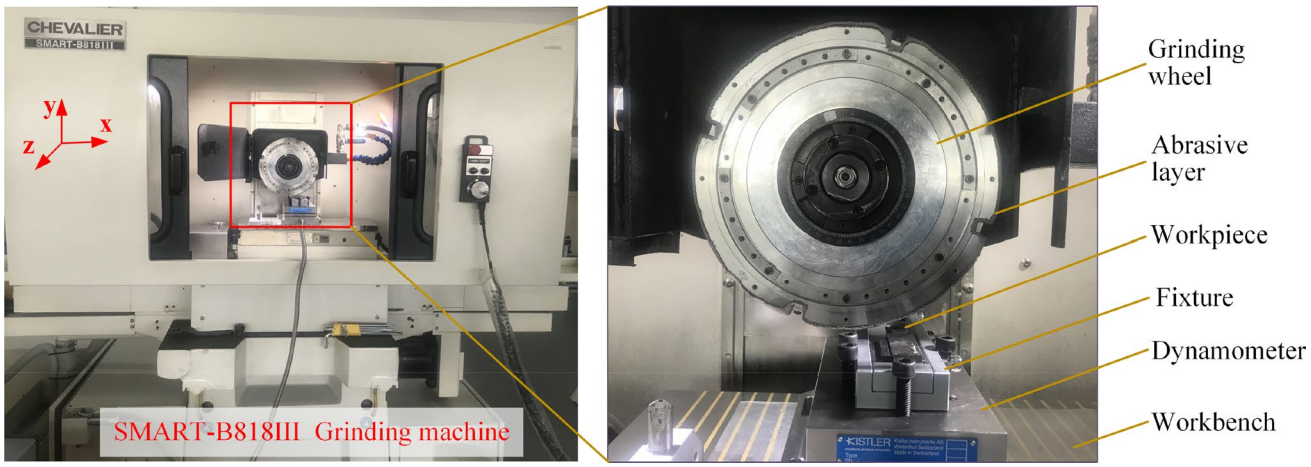

Fig. 4 Experimental setup

Table 1 Experimental parameters

Items	Parameters
Dispersion medium	PEG200
Dispersed phase (15 wt%)	SiO_2
Polymer polyethylene fibers	UHMWPEF
Type of abrasive	Al_2O_3, SiC, CBN
Size of abrasive particle (μm)	1, 10, 20
Abrasive particle percentage in STAF (wt%)	5, 10, 15
Workpiece material	Inconel718
Initial surface roughness of workpiece (μm)	~0.3
Grinding speed v_s (m/s)	5
Feed speed v_w (mm/min)	500
Cutting depth a_p (μm)	250

force. During grinding process, a_p remained unchanged. The grinding conditions were summarized in Table 1.

2.4 Assessment of material removal rate

The abrasive layer of the liquid-body-armor-like grinding wheel would have a bigger deformation during HSLP grinding, which was different from that during the conventional grinding, as shown in Fig. 5. Therefore, the deformation of the abrasive layer could not be ignored. *MRR* is calculated as follows.

$$t_0 = \frac{l_w}{v_w} \tag{1}$$

$$t_c = 250 \times t_0 \tag{2}$$

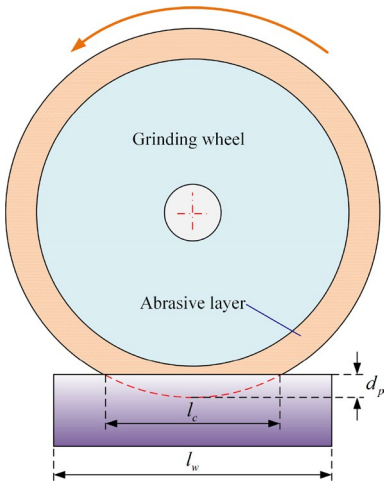

Fig. 5 Diagram of contact state between grinding wheel and workpiece

$$MRR = \frac{m_b - m_a}{\rho_w \times z \times t_c} \tag{3}$$

where l_w is the length of workpiece. z is the width of grinding zone. t_0 represents the contact time during a grinding stroke. t_c represents the total contact time in 250 grinding strokes. m_b and m_a are the workpiece mass before and after grinding, respectively. ρ_w is the density of workpiece.

2.5 Autocorrelation function of surface profile

In the traditional grinding process, the material removal mechanism, the surface formation mechanism, and the abrasive wear condition, et al. could be revealed though direct 2D

measurement results (e.g., surface roughness, surface morphology, et al.). However, the contact state between the novel wheel and workpiece surface becomes more complicated. As the rotated wheel contacting the workpiece surface, solid-like abrasive particle clusters are generated in the grinding zone. While, abrasive particle clusters are dispersed into many single abrasive particles immediately when leaving the grinding zone. Moreover, the flow behavior of the single abrasive particle occurred in the non-grinding zone. Furthermore, the removed debris may be left on the abrasive layer, an unpredicted formation on the workpiece surface may be produced. To obtain more microstructure information, the autocorrelation function (ACF) was used to express the similarity of phase difference displacement τ at the same contour waveform, as calculated in Eq. (4) [14]. It provided a new approach to exploring the surface formation mechanism in HSLP grinding process.

$$R_x(\tau) = \frac{1}{L}\int_0^L x(t)x(t+\tau)dt \tag{4}$$

where τ is the displacement. $x(t)$ is the surface profile curve. L is the sampling length.

The digital estimation was obtained as:

$$ACF(rh) = \frac{1}{N-r}\sum_{n=0}^{N-r-1} Y_n Y_{n+r}(r = 0, 1, 2, 3.....m, m < n) \tag{5}$$

where r is the transverse displacement number. h is the sample interval. m is the maximum displacement number. N is the sampling capacity.

2.6 Power spectral density function of surface profile

Furthermore, the power spectral density (PSD) function was used to disclose the percentage of waviness and roughness of the surface profile. PSD described the randomness of profile in the frequency domain. Amplitude expressed relative frequency proportions under different frequencies. It can elucidate the variation principle of the surface under different grinding wheel parameters, identify surface formation mechanism in HSLP grinding process, obtained as following function [28].

$$PSD\ (f) = \frac{1}{\Delta f}\left[\frac{1}{L}\int_0^L y^2(x, f, \Delta f)dx\right] \tag{6}$$

where L is the evaluation length. $y^2(x, f, \Delta f)$ is the squared value of $y(x)$ in the range of $f \sim (f + \Delta f)$.

The standard Fourier transform method was used to calculate PSD, as follows:

$$G_x\ (f_x) = 2h\left[R_0 + 2\sum_{r=1}^{m-1} R_r \cos\left(\frac{\pi kr}{m}\right) + (-1)^k R_m\right] \quad (k = 0, 1, 2, 3, ..., m-1) \tag{7}$$

where h is the sample interval. m is the sample capacity.

3 Results and discussions

3.1 Variations of abrasive particle types

Figure 6 illuminates the variation of *Ra* and *MRR* with different types of abrasive particles (Al_2O_3, SiC and CBN) used by the liquid-body-armor-like grinding wheel. The average abrasive particle size and abrasive particle percentage was 1 μm and 5 wt%, respectively. The grinding parameters were kept at a feed speed of 500 mm/min, wheel speed of 5 m/s, and cutting depth of 250 μm, respectively. From Fig. 6, it could be seen that the *Ra* and *MRR* were greatly affected by the abrasive type. *Ra* was reduced to 0.112 μm, 0.183 μm, and 0.094 μm for Al_2O_3, SiC, and CBN grinding wheel after processing from the initial value, 0.3 μm, respectively. The fact that the developed CBN grinding wheel helped obtain the ultra-refining surface was demonstrated. *Ra* was improved by 69%. *MRR* obtained by three different abrasive

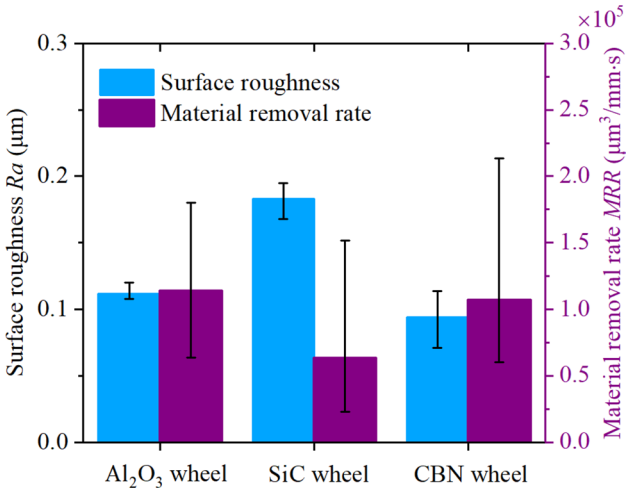

Fig. 6 *Ra* and *MRR* variations for different abrasive particle types

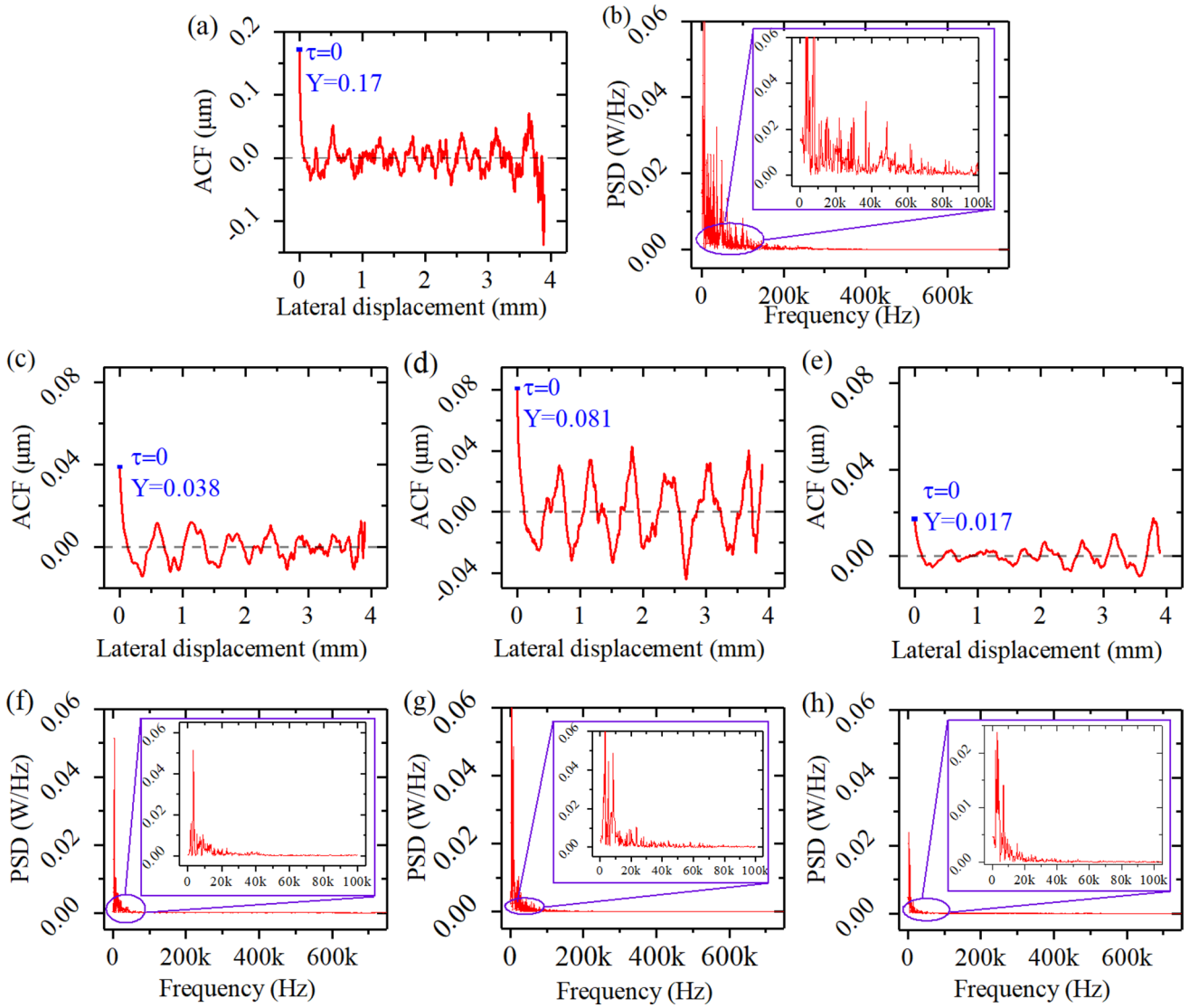

Fig. 7 Workpiece surface profile analysis of **a** ACF curve and **b** PSD curve before grinding, **c** ACF curve using Al_2O_3 wheel, **d** ACF curve using SiC wheel, **e** ACF curve using CBN wheel, **f** PSD curve using Al_2O_3 wheel, **g** PSD curve using SiC wheel and **h** PSD curve using CBN wheel after grinding

type were 1.128×10^5 μm^3/mm·s, 0.634×10^5 μm^3/mm·s, 1.069×10^5 μm^3/mm·s, respectively.

The ACF curves and PSD curves of workpiece surface profiles after grinding using the developed Al_2O_3, SiC and CBN wheels are shown in Fig. 7. It was found that the ACF value was maximum at $\tau = 0$ after grinding. The maximum value in Fig. 7(c), (d) and (e), reached 0.038, 0.081, and 0.017 using Al_2O_3, SiC and CBN wheels, respectively. Compared with the initial value (0.17) before grinding, in Fig. 7(a), it had a great diminution after grinding. According to the relationship between ACF and Y_nY_{n+1}, the smaller ACF, the better surface quality. Therefore, ACF results showed that the surface quality could be improved by HSLP grinding using the liquid-body-armor-like grinding wheel. Moreover, the CBN grinding wheel was verified to be better, which was consistent with *Ra* in Fig. 6. On the other hand, with the increase of the lateral displacement, the ACF curves faded away rapidly. Simultaneously, a periodic reverberation occurred and kept on for the three wheels. An interest phenomenon that the oscillation period of the three curves was larger than that of before grinding needed to be paid attentions.

The PSD curves of the workpiece surface after grinding were studied to clarify the periodic change law of surface profile. It was obvious that the PSD curves in Fig. 7(b), (f–h) rapidly decreased with the increase in frequency. The amplitude of the PSD curve denoted relative frequency proportions at different frequencies. A long period was

associated with a low frequency. Compared with the PSD curve before grinding, the reverberation of curves after grinding was mainly concentrated in the low-frequency domain. It revealed that the long period surface profile was generated in the HSLP grinding process. The clustering effect of the abrasive particles could be verified to some extent. Moreover, the PSD curves in Fig. 7(f and h) were concentrated in 0–40 k Hz. However, although the curve in Fig. 7(g) was mainly concentrated in 0–40 k Hz, distribution in higher frequency domain was also discovered. The interesting findings reflected that the abrasive particle cluster size was also different from each other with varies abrasive types of grinding wheel in the HSLP grinding process.

According to the above analysis on the ACF curves and PSDF curves from Fig. 7, as well as *Ra* and *MRR* curves in Fig. 6, the workpiece surface formation mechanism in the HSLP grinding process with different wheels are exhibited in Fig. 8. The curves using Al_2O_3 wheel and CBN wheel mainly concentrated in the low-frequency domain, which signified that a larger abrasive particle cluster was generated in the grinding zone, as shown in Fig. 8(a) and (c). In addition, lower hardness of Al_2O_3 abrasive particle for machining Inconel718 alloy, which led to unpredicted wear during grinding process. The micro-fracture debris of the abrasive is illuminated in Fig. 8(a). It caused the *Ra* obtained the Al_2O_3 wheel to be slightly larger than that using the CBN wheel. Moreover, the relatively weak rheological property of the SiC abrasive fluid caused a much smaller diameter of the abrasive particle clustering than that of the others, as shown in Fig. 8(b). The smaller diameter caused the distribution of PSD curve to be in a higher frequency domain. Meanwhile, the processing capacity was reduced, leading to a higher *Ra* and a lower *MRR* using the SiC wheel. According to the above analysis, the surface formation mechanism in HSLP grinding process with different wheels was clarified. The influence law of different abrasive type on grinding characteristics could be understood fully. The CBN wheel was found to be suitable for machining Inconel718 alloy in the HSLP grinding process.

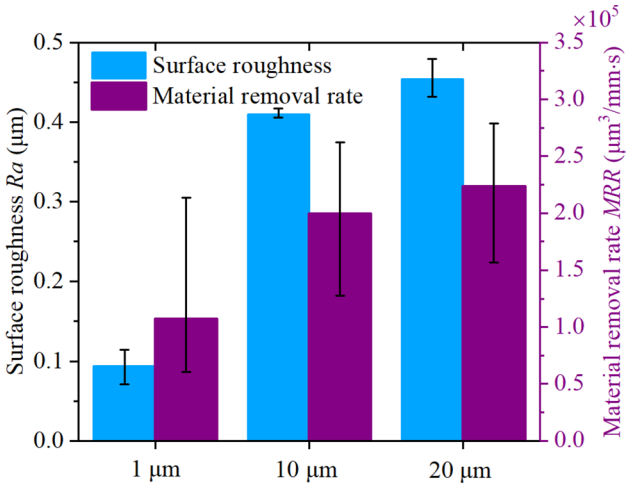

Fig. 9 *Ra* and *MRR* variations for different abrasive particle size

3.2 Variations of abrasive particle sizes

Figure 9 presents the variation of *Ra* and *MRR* with different abrasive particle sizes (1 μm, 10 μm, 20 μm). An abrasive particle percentage of 5 wt% was used. The grinding parameters were kept. *Ra* reached 0.094 μm at 1 μm, 0.410 μm at 10 μm, and 0.454 μm at 20 μm after grinding, respectively. It indicated that the CBN grinding wheel at 1 μm helped achieve in obtaining ultra-refining surface. It was obvious that the *Ra* was greatly affected by the abrasive size. A more interesting phenomenon was that *Ra* after grinding at the size of 10 μm and 20 μm was larger than that before grinding. Further analysis would be carried out in the next section to explain this phenomenon. Meanwhile, *MRR* in different abrasive particle sizes were 1.069×10^5 μm³/mm·s,

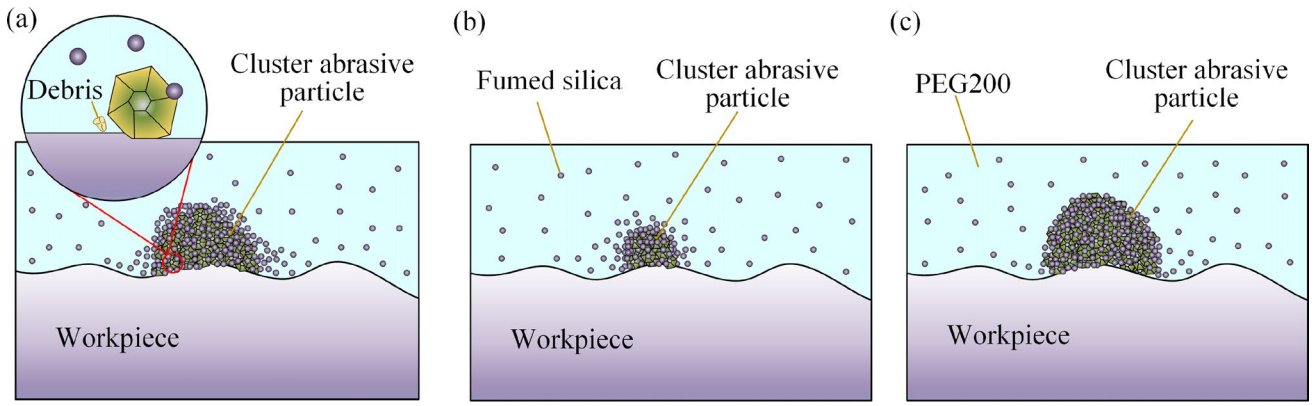

Fig. 8 Surface formation mechanism in grinding process: **a** with Al_2O_3 wheel, **b** with SiC wheel, and **c** with CBN wheel

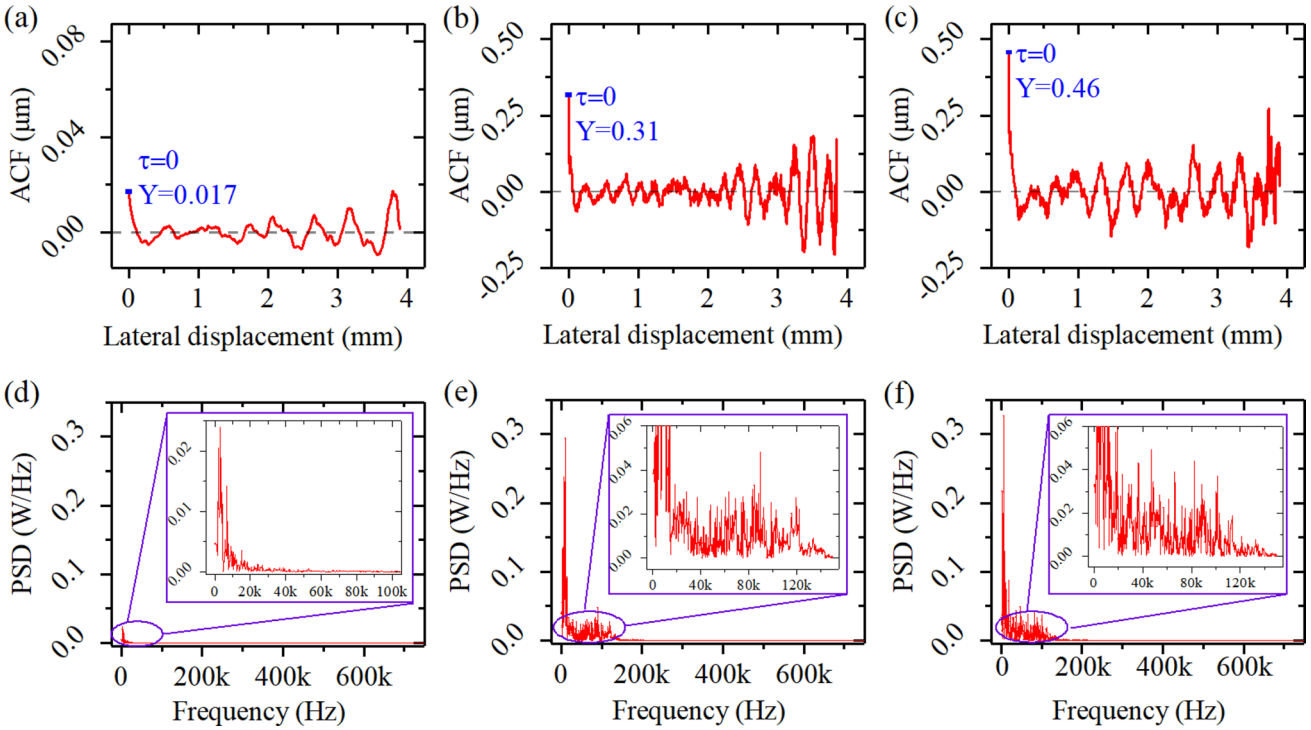

Fig. 10 Workpiece surface profile analysis of **a** ACF curve at 1 μm, **b** ACF curve at 10 μm, **c** ACF curve at 20 μm, **d** PSD curve at 1 μm, **e** PSD curve at 10 μm, and **f** PSD curve at 20 μm using CBN wheel after grinding

1.992×10^5 μm^3/mm·s, 2.230×10^5 μm^3/mm·s, respectively. The ultra-refining surface but a minimum *MRR* was obtained at the same grinding conditions.

Figure 10 displays the ACF curves and PSD curves of workpiece surface profiles after grinding with the CBN wheel at an abrasive particle size of 1 μm, 10 μm and 20 μm, respectively. It was found that the maximum ACF values in Fig. 10(a), (b) and (c) reached 0.017, 0.31, and 0.46, respectively. The ACF value at 1 μm was much smaller than that (0.17) before grinding, while, the others at 10 μm and 20 μm were much greater than that before grinding. The ACF results were consistent with the analysis results of *Ra* in Fig. 9. Similarly, the three curves remained a periodic reverberation with amplitudes, indicating that the workpiece surface profile changed periodically. Moreover, the periods of the three curves were different. The longest period occurred at the smallest size (1 μm). The shortest period was gained with the middle size (10 μm), rather than the biggest size (20 μm). The findings were interesting enough to deserve further analysis.

The PSD curves of the workpiece surface after grinding with the CBN wheel at an abrasive particle size of 1 μm, 10 μm and 20 μm are shown in Fig. 10(d), (e) and (f), respectively. The PSD curves were mainly concentrated in the low-frequency domain. It was obvious that the PSD curve in in Fig. 10(d) was mainly concentrated within 0–40 k Hz, signifying longer periods of this surface profile. Figure 10(e) displays the curve been concentrated within 0–130 k Hz. While a concentration within 0–115 k Hz of the curve using a 20 μm CBN wheel is illuminated in Fig. 10(f). It indicated

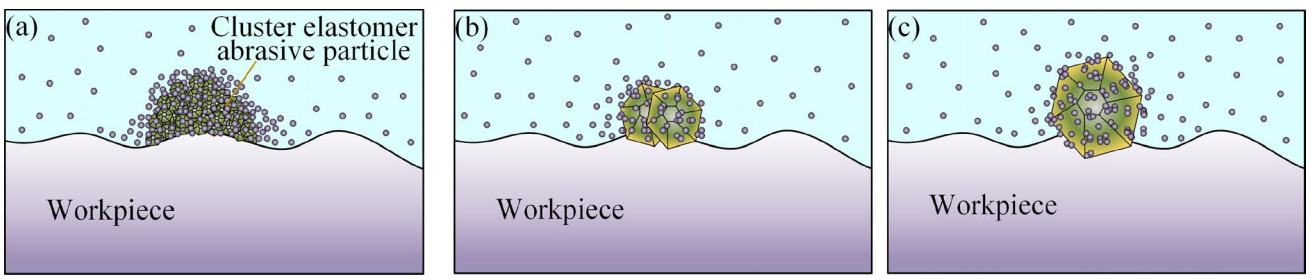

Fig. 11 Surface formation mechanism in grinding process for **a** with 1 μm, **b** 10 μm, and **c** 20 μm CBN wheel

that a shorter period existed in Fig. 10(e), compared to that of Fig. 10(f). The interesting discovery reflected the different abrasive particle clustering states.

The workpiece surface formation mechanisms in the HSLP grinding process with the different abrasive particle sizes of the CBN grinding wheel are exhibited in Fig. 11. A low frequency was associated with a big abrasive particle cluster, like Fig. 11(a). The bigger cluster abrasive particle was generated in the grinding zone at 1 μm. Similarly, the curves for 10 μm and 20 μm concentrated in the high frequency domain, reflecting the existence of some smaller abrasive particle clusters, like Fig. 11(b) and (c). However, a phenomenon that the smallest *MRR* was obtained due to the bigger cluster abrasive particle needed to be paid more attention to, as shown in Fig. 9. It was attributed by the fact that the big cluster abrasive particle was characterized by the elasticity, namely the cluster elastomer abrasive particle. Under the normal pressure of the abrasive layer, the cluster elastomer abrasive particle deformed, then the micro-profile of the workpiece surface was adaptive, as displayed in Fig. 11(a). The material removal efficiency was thus reduced. The workpiece surface quality was, however, improved. However, the abrasive fluids with 10 μm and 20 μm CBN abrasive particles displayed a relatively weak rheological property. A smaller diameter of cluster abrasive particles was created in the grinding zone, as illuminated in Fig. 11(b) and (c). The smaller deformation occurred for those cluster abrasive particles under the pressure of the abrasive layer. It was helpful for the single particle of those cluster abrasive particles penetrating the workpiece surface, improving the *MRR*. The poor surface quality, but high *MRR* with big size CBN abrasive particle was explained in the HSLP grinding process. Therefore, the CBN wheel in 1 μm abrasive particle was better for grinding Inconel718 alloy using the HSLP grinding method.

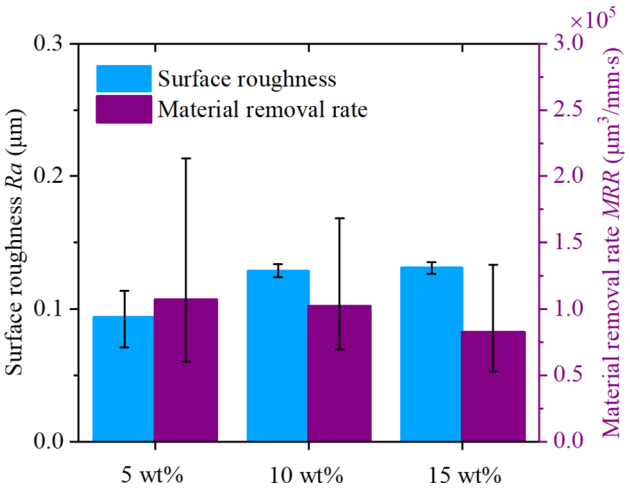

Fig. 12 *Ra* and *MRR* variations for different abrasive mass percentages

3.3 Variations of abrasive percentages

Figure 12 displays the variation of *Ra* and *MRR* with different abrasive percentages (5 wt%, 10 wt%, 15 wt%) in the CBN grinding wheel. CBN abrasive particle of 1 μm was adopted. *Ra* reached 0.094 μm with 5 wt%, 0.129 μm with 10 wt%, 0.131 μm with 15 wt% after grinding from the original 0.3 μm, respectively. *Ra* had a significantly change with abrasive percentages in the HSLP grinding process. Among the three abrasive percentages, the grinding wheel with 5 wt% was useful to obtain an ultra-refining surface, which was improved by 69%. Meanwhile, *MRR* reached 1.069×10^5 $\mu m^3/mm{\cdot}s$, 1.022×10^5 $\mu m^3/mm{\cdot}s$, and 0.825×10^5 $\mu m^3/mm{\cdot}s$, respectively. It was found that the ultra-refining surface with a higher *MRR* was grained using grinding wheel of 5 wt% abrasive percentage.

Figure 13 displays the ACF curves and PSD curves of the workpiece surface after grinding with different abrasive percentages (5 wt% 10 wt% and 15 wt%) in the CBN wheel, respectively. From Fig. 13(a), (b) and (c), it was obvious that the maximum values of the ACF curves were smaller than that (0.17) before grinding, being consistent with the *Ra* in Fig. 12. Secondly, the ACF curves remained a periodic reverberation with amplitudes. Reverberation indicated that the workpiece surface profile changed periodically. Among the three curves, the longest period was obtained when using the minimum percentage (5 wt%). Meanwhile, the shortest one was gained in the maximum percentage (15 wt%). In addition, the PSD curves were mainly concentrated within 0 ~ 40 k Hz, signifying the existence of many long periods in those surface profiles. Figure 13(e) and (f) show the curve is distributed within 0–80 k Hz. While, a scattered distribution in 80–110 k Hz had occurred in the latter case, as illuminated in Fig. 13(f). The abrasive particle cluster station with a variation of abrasive particle percentage was different.

The high frequency indicated a small cluster of abrasive particles, whereas a low frequency meant a big cluster. The workpiece surface formation mechanism with different abrasive particle percentages was shown in Fig. 14. Due to the different rheological properties of the three abrasive fluids, the diameter of cluster abrasive particle in the grinding zone decreased with the increased abrasive percentage. *MRR* was thus decreased. Furthermore, the cluster abrasive particle was characterized by elasticity. Under the normal pressure of the abrasive layer, the shape cluster abrasive particle was adaptive to the micro-profile of the workpiece surface. Both *MRR* and workpiece surface quality were improved in the bigger cluster of abrasive particles.

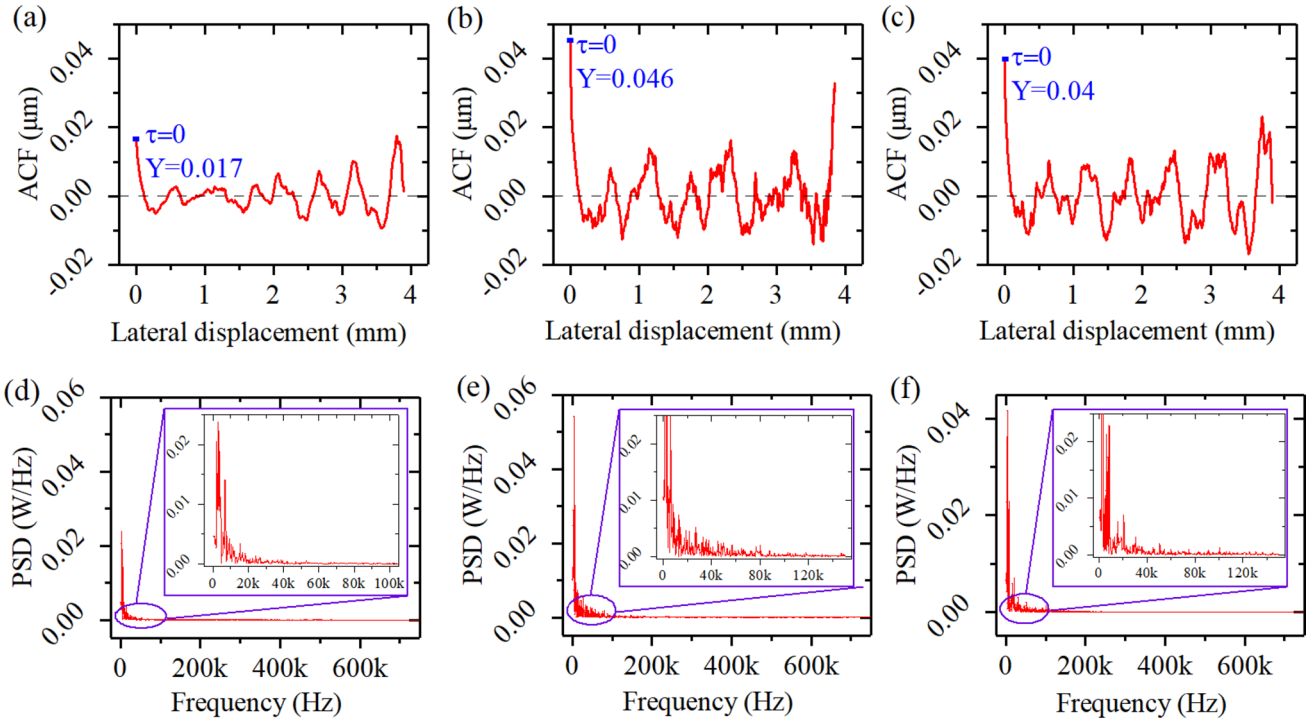

Fig. 13 Workpiece surface profile analysis of **a** ACF curve with 5 wt%, **b** ACF curve with 10 wt%, **c** ACF curve with 15 wt%, **d** PSD curve with 5 wt%, **e** PSD curve with 10 wt%, and **f** PSD curve with 15 wt% abrasive particles in CBN wheel after grinding

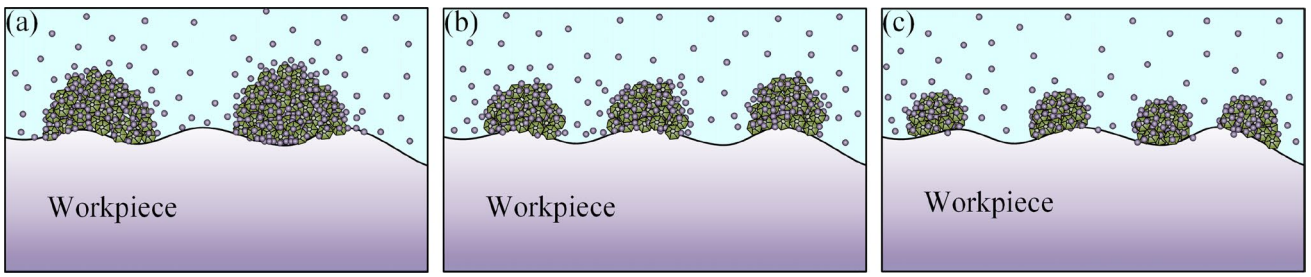

Fig. 14 Surface formation mechanism in grinding process for **a** 5 wt%, **b** 10 wt%, and **c** 15 wt% abrasive particle percentage in CBN wheel

According to the above analysis, the influences of abrasive particle material types, sizes and percentages on *Ra* and *MRR* have been revealed well. The surface formation mechanism in the HSLP grinding process was explained from the view of the particle cluster. The optimized abrasive type, size, and mass percentage were finally obtained to be CBN, 1 μm, and percentage of 5 wt%, respectively.

3.4 Surface observation

To further understand the grinding performance of the HSLP grinding process, the surface morphology was investigated by field-emission scanning electron microscopy (FEI Sirion 200, Unite States). The samples were cleaned by an ultrasonic cleaner for SEM test preparation. Figure 15 shows the variations in SEM morphology. The

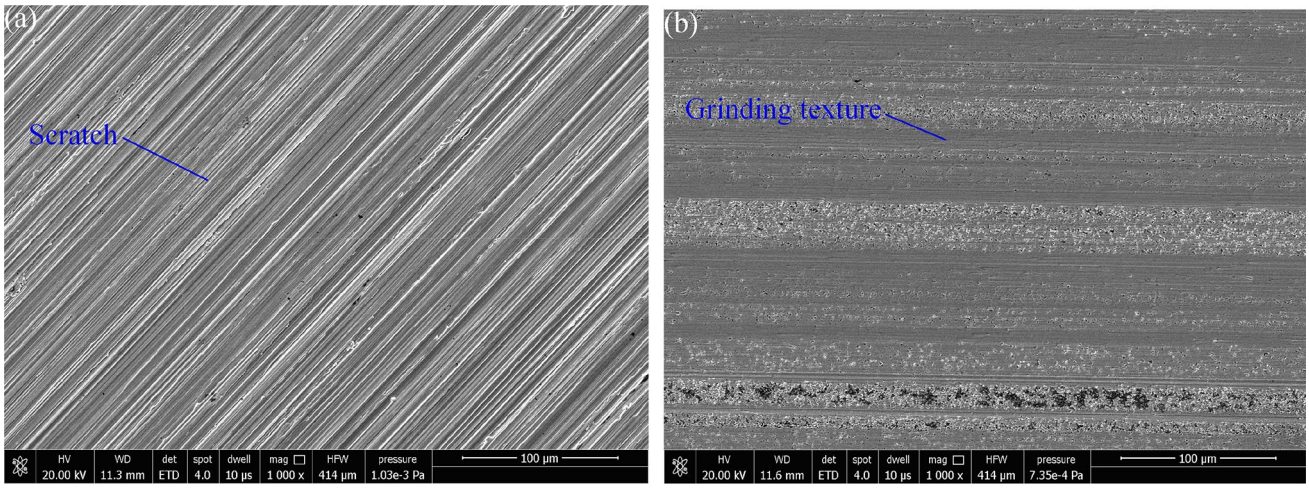

Fig. 15 SEM micrographs of workpiece surface for **a** before grinding and **b** after grinding

surface before grinding has numerous deep scratches, as shown in Fig. 15(a). No scratches were left on the surface after grinding, as seen from Fig. 15(b). A smooth surface was obtained. The shallow grinding texture was produced. It was worth noticing that white banded stripes exist due to the waviness of polymer polyethylene fibers used in the abrasive layer. The SEM observation results indicated that the optimized grinding wheel was useful to machine Inconel718 with better surface quality and higher material removal efficiency.

4 Conclusions

In this work, an experimental investigation was presented to study how the abrasive type, size, and mass percentage affect the surface quality and material removal efficiency. The variation of *Ra*, *MRR*, ACF, and PSD with wheel parameters in the HSLP grinding process were analyzed. The workpiece surface formation mechanism was explained from the view of the particle clustering. The following conclusions could be obtained.

(1) The abrasive particle type, size, and mass percentage of the developed grinding wheel have a significant influence on *Ra* and *MRR* in the HSLP grinding process. Among the three abrasive particle types (Al_2O_3, SiC and CBN), a refine surface was obtained by the CBN abrasive particle. Using the CBN liquid-body-armor-like grinding wheel, *MRR* and *Ra* increased with the raised particle size, respectively. On the aspect of the mass percentage, *Ra* varied significantly, while, *MRR* had no obvious change. The optimal combination of type, size, and mass percentage were CBN, 1 µm, and 5 wt%, respectively.

(2) After the wheel parameter optimization, the initial scratches on the surface of Inconel718 alloy were removed. The grinding textures were visible. Its surface roughness was reduced to 0.094 µm, which was improved by 69%. Meanwhile, the *MRR* reached 1.069×105 µm^3/mm·s.

(3) The microstructure information of the workpiece surface profile before and after grinding was analyzed through the ACF method. With the optimal wheel parameters, the maximum ACF was 0.017, had a great diminution compared with the initial value (0.17) before grinding. It was further verified that the optimized grinding wheel was useful to machine Inconel718 alloy in the HSLP grinding process.

(4) The surface variation rules were further analyzed through the PSD method. The PSD of surface profile curves was different in varied abrasive material types, sizes, and mass percentages. A bigger cluster of elastomer abrasive particles was generated in the grinding zone using the optimized grinding wheel.

Acknowledgements This work was financially supported by the National Natural Science Foundation of China (Nos. 51875329 and 51905322), Shandong Provincial Natural Science Foundation (No. ZR2023ME112), Taishan Scholar Project of Shandong Province (No. tsqn201812064), Science and Technology Support Plan for Youth Innovation of Colleges and Universities of Shandong Province of China (No. 2019KJB030), Innovation Capacity Improvement Programme for High-tech SMEs of Shandong Province (Nos. 2022TSGC1333, 2022TSGC1261).

Author contributions BL: Writing-original draft (lead), Formal analysis (lead), Visualization (lead), Writing-review and editing (supporting). YT: Supervision (lead), Conceptualization (lead), Writing-review and editing (lead). JH: Supervision (supporting), Writing-review and editing (supporting). JW: Writing-review and editing (supporting), Visualization (supporting). GZ: Visualization (supporting). ZG: Visualization (supporting).

Declarations

Conflict of interest The author(s) declared no potential conflicts of interest with respect to the research, authorship, and/or publication of this article.

References

1. Ghosh S, Chattopadhyay AB, Paul S (2008) Modelling of specific energy requirement during high-efficiency deep grinding. Int J Mach Tool Manuf 48:1242–1253. https://doi.org/10.1016/j.ijmachtools.2008.03.008
2. Xiao GD, Zhao B, Ding WF, Huang HX (2021) On the grinding performance of metal-bonded aggregated cBN grinding wheels based on open-pore structures. Ceram Int 47:19709–19715. https://doi.org/10.1016/j.ceramint.2021.04.001
3. Mohamed AM, Bauer R, Warkentin A (2013) Application of shallow circumferential grooved wheels to creep-feed grinding. J Mater Process Tech 213:700–706. https://doi.org/10.1016/j.jmatprotec.2012.11.029
4. Zhang SQ, Yang ZX, Jiang RS, Jin QC, Zhang Q, Wang WH (2021) Effect of creep feed grinding on surface integrity and fatigue life of Ni3Al based superalloy IC10. Chin J Aeronaut 34:438–448. https://doi.org/10.1016/j.cja.2020.02.025
5. Hood R, Cooper P, Aspinwall DK, Soo SL, Lee DS (2015) Creep feed grinding of γ-TiAl using single layer electroplated diamond superabrasive wheels. Ann CIRP 11:36–44. https://doi.org/10.1016/j.cirpj.2015.07.001
6. Yang L, Fu YC, Xu JH, Liu YT (2015) Structural design of a carbon fiber-reinforced polymer wheel for ultra-high speed grinding. Mater Des 88:827–836. https://doi.org/10.1016/j.matdes.2015.09.066
7. Wu Y, Lu P, Lin FH, Bao WC, Qu MN, Li P, He H (2021) Explosion accident analysis of ultra-high-speed grinding wheel. Eng Fail Anal 122:105209. https://doi.org/10.1016/j.engfailanal.2020.105209
8. Bell A, Jin T, Stephenson DJ (2011) Burn threshold prediction for high efficiency deep grinding. Int J Mach Tool Manuf 51:433–438. https://doi.org/10.1016/j.ijmachtools.2011.01.006
9. Tawakoli T, Azarhoushang B (2011) Intermittent grinding of ceramic matrix composites (CMCs) utilizing a developed segmented wheel. Int J Mach Tool Manuf 51:112–119. https://doi.org/10.1016/j.ijmachtools.2010.11.002
10. Li HN, Axinte D (2016) Textured grinding wheels: a review. Int J Mach Tool Manuf 109:8–35. https://doi.org/10.1016/j.ijmachtools.2016.07.001
11. Vardhanapu M, Chaganti PK, Tarigopula P (2023) Characterization and machine learning-based parameter estimation in MQL machining of a superalloy for developed green nano-metalworking fluids. J Braz Soc Mech Sci Eng 45:154. https://doi.org/10.1007/s40430-023-04078-0
12. Babu MN, Anandan V, Parthasarathi NL, Yildirim CV, Babu MD, Das SR (2022) Performance analysis in turning of D3 tool steel using silver nanoplatelets as additives under MQL. J Braz Soc Mech Sci Eng 44:591. https://doi.org/10.1007/s40430-022-03909-w
13. Mao C, Zhou X, Yin LR, Zhang MJ, Tang K, Zhang J (2016) Investigation of the flow field for a double-outlet nozzle during minimum quantity lubrication grinding. Int J Adv Manuf Technol 85:291–298. https://doi.org/10.1007/s00170-015-7896-2
14. Zhang XP, Li CH, Zhang YB, Wang YG, Li BK, Yang M, Guo SM, Liu GT, Zhang NQ (2017) Lubricating property of MQL grinding of Al_2O_3/SiC mixed nanofluid with different particle sizes and microtopography analysis by cross-correlation. Precis Eng 47:532–545. https://doi.org/10.1016/j.precisioneng.2016.09.016
15. Hadad MJ, Tawakoli T, Sadeghi MH, Sadeghi B (2012) Temperature and energy partition in minimum quantity lubrication-MQL grinding process. Int J Mach Tool Manuf 54–55:10–17. https://doi.org/10.1016/j.ijmachtools.2011.11.010
16. Zhu WL, Beaucamp A (2020) Compliant grinding and polishing: a review. Int J Mach Tool Manuf 158:103634. https://doi.org/10.1016/j.ijmachtools.2020.103634
17. Beaucamp A, Namba Y, Combrinck H, Charlton P, Freeman R (2014) Shape adaptive grinding of CVD silicon carbide. Ann CIRP 63:317–320. https://doi.org/10.1016/j.cirp.2014.03.019
18. Wang C, Wu YR, Liao HZ, Deng C, Luo J, Huang Y (2022) Influence of contact force and rubber wheel hardness on material removal abrasive blet grinding investigated by physical simulator. Precis Eng 78:70–78. https://doi.org/10.1016/j.precisioneng.2022.07.009
19. Xiao GJ, Chen BQ, Li SC, Zhuo XQ, Zhao ZY (2022) Surface integrity and fatigue performance of GH4169 superalloy using abrasive belt grinding. Eng Fail Anal 142:106764. https://doi.org/10.1016/j.engfailanal.2022.106764
20. Ge YC, Zhu ZW, Wang DY, Ma Z, Zhu D (2019) Study on material removal of electrochemical deep grinding. J Mater Process Tech 271:510–519. https://doi.org/10.1016/j.jmatprotec.2019.04.033
21. Cao Y, Ding WF, Zhao B, Wen XB, Li SP, Wang JZ (2022) Effect of intermittent cutting behavior on the ultrasonic vibration-assisted grinding performance of Inconel718 nickel-based superalloy. Precis Eng 78:248–260. https://doi.org/10.1016/j.precisioneng.2022.08.006
22. Chen Y, Hu ZW, Yu YQ, Yu YQ, Lai ZY, Zhu JG, Xu XP, Peng Q (2022) Processing and machining mechanism of ultrasonic vibration-assisted grinding on sapphire. Mater Sci Semi Process 142:106470. https://doi.org/10.1016/j.mssp.2022.106470
23. Aurich JC, Dornfeld D, Arrazola PJ, Franke V, Leitz L, Min S (2009) Burrs—Analysis, control and removal. Ann CIRP 58:519–542. https://doi.org/10.1016/j.cirp.2009.09.004
24. Kaliszer H (1991) Grinding technology. Theory and applications of machining with abrasive. Int J Mach Tool Manuf 31(3):435–436. https://doi.org/10.1016/0890-6955(91)90088-K
25. Tian YB, Li LG, Fan S, Guo QJ, Cheng X (2020) A novel high-shear and low-pressure grinding method using specially developed abrasive tools. Proc IMechE Part B: J Eng Manuf 235:166–172. https://doi.org/10.1177/0954405420949106
26. Tian YB, Li LG, Han JG, Fan ZH, Liu K (2020) Development of novel high-shear and low-pressure grinding tool with flexible

composite. Mater Manuf Process 36:479–487. https://doi.org/10.1080/10426914.2020.1843673
27. Liu B, Tian YB, Han JG, Li LG, Gu ZQ, Hu XT (2022) Development of a new high-shear and low-pressure grinding wheel and its grinding characteristics for Inconel718 alloy. Chin J Aeronaut 35(12):278–286. https://doi.org/10.1016/j.cja.2021.08.013
28. Zhang XP, Li CH, Jia DZ, Gao T, Zhang YB, Yang M, Li RZ, Han ZG, Ji HJ (2019) Spraying parameter optimization and microtopography evaluation in nanofluid minimum quantity lubrication grinding. Int J Adv Manuf Technol 103:2523–2539. https://doi.org/10.1007/s00170-019-03642-0